INSTITUTE OF PHYSICS PUBLISHING JOURNAL OF PHYSICS: CONDENSED MATTER

J. Phys.: Condens. Matter **17** (2005) 6519–6531 doi:10.1088/0953-8984/17/41/021

Detailed magnetic dynamic behaviour of nanocomposite iron oxide aerogels

M B Fernández van Raap[1], F H Sánchez[1], C E Rodríguez Torres[1], Ll Casas[2], A Roig[2] and E Molins[2]

[1] Departamento de Física, Facultad de Ciencias Exactas, Universidad Nacional de La Plata, C.C. 67 (1900) La Plata, Argentina
[2] Institut de Ciència de Materials de Barcelona (ICMAB-CSIC), Campus UAB, 08193 Bellaterra, Catalunya, Spain

Received 12 April 2005, in final form 29 August 2005
Published 30 September 2005
Online at stacks.iop.org/JPhysCM/17/6519

Abstract

The magnetic properties of maghemite particles hosted in silica aerogel pores are studied in depth, with most of the focus on the magnetic relaxation mechanisms. It is shown that at room temperature, the system behaves as an ensemble of non-interacting superparamagnetic particles, indicating that particle aggregation can be avoided by using a sol–gel preparation method with supercritical drying. In the temperature range from 15 to 300 K the magnetic ac susceptibility $\chi(T)$ displays a broad peak that shifts to higher temperatures on increasing the ac applied field frequency. Transmission electron microscopy reveals acicular shaped maghemite particles exhibiting unimodal size distributions, from which energy barrier distributions can be inferred. The distribution of activation energies has been independently obtained from scaling plots of the frequency dependent out-of-phase ac susceptibility component using $\tau_0 = 10^{-11}$ s. The value obtained is in agreement with the one derived from the particle size distribution. Combining the two distributions and assuming magnetic volume anisotropy, an effective anisotropy constant $K_{\mathrm{eff}} \cong 1.02$–$1.4 \times 10^5$ J m^{-3} was determined for 5×20 nm and 4×20 nm average dimensions respectively. It is also shown that the temperature dependences of the relaxation time τ as obtained from Néel analysis of the magnetic absorption $\chi''(T, \omega)$ and Cole–Cole frequency dependence analysis are in good agreement with the value derived from Mössbauer effect spectroscopy at room temperature.

1. Introduction

Silica aerogels are sol–gel derived nanostructured materials that exhibit an accessible internal porous structure. Due to their high porosity, they present very low densities ($\rho = 0.04$–0.6 g cm^{-3}) and high specific surfaces. These materials are thermally insulating and optically transparent with low dielectric constant.

Their various potential applications have been increased by trapping nanosized magnetic particles in their internal porous structure [1–4]. Recent investigations suggest that ultralight transparent magnets could be developed in the near future [5]. On the other hand, the preparation of magnetic nanocomposite aerogels under especially shaped external fields opens the possibility of designing patterned magnetic nanostructures under specific preparation conditions [6]. The resulting material consists of a dispersed nanocrystalline magnetic phase hosted in an electrically insulating silica matrix. Magnetic particle size can be tailored, avoiding or promoting aggregation. As the magnetic particles are in the nanometre range, their properties may differ from those of the bulk magnets due to their single-domain nature and the higher proportion of atoms located at their surfaces. A surface effect leading to a smaller net magnetic moment per particle and net anisotropy exceeding the bulk values has been reported for nanocomposite materials prepared by other methods like sequential sputtering deposition of Co and Al_2O_3 [7].

The purpose of the present work is the study of magnetic relaxation effects in nanocomposite iron oxide/silica aerogels. The knowledge of the magnetic dynamic behaviour of these materials and the development of methods for its modification are important for their potential applications as magneto-optical devices.

We thus present here an ac susceptibility study on maghemite particles hosted in silica aerogel pores prepared by the sol–gel method; the samples were previously described in [8]. This paper focuses on ac susceptibility studies of maghemite-bearing aerogels (samples labelled as A3 and B2), and results from ferrihydrite aerogels (the sample labelled as A1) will be commented on only for comparison when appropriate. Some interesting results for sample A1, obtained using Mössbauer effect (ME) spectroscopy under an external magnetic field, were already presented in [1] (notice that in this reference the material was labelled as B1).

As the ac susceptibility analysis employed here is applicable only if the samples contain magnetic particles of one type, we will briefly review the characterization related to phase assignment and morphology and then we will discuss the ac susceptibility results. We will also show that the results derived using the Néel model or by scaling frequency dependent curves for χ'' are consistent with the ones obtained by applying Argand plots assuming a Cole–Cole expression.

2. Experimental details

Details on the preparation of the materials used can be found elsewhere [8]. Summarizing, the material was obtained via sol–gel hydrolysis/condensation reactions of a silicon alkoxide $Si(OCH_2CH_3)_4$ (TEOS) or $Si(OCH_3)_4$ (TMOS) with water in an alcoholic solvent. The drying was achieved by supercritical evacuation of the solvent in a computer-controlled high temperature and high pressure plant. Two different precursors were used to grow the magnetic phase into the silica aerogel:

(a) A 1.5 M solution of hydrated iron salt ($Fe(NO_3)_3{\cdot}9H_2O$) dissolved in an alcohol was added to the silicon alkoxide promoting polymerization of both the silica matrix and iron oxide (sample A1 using TEOS and A3 using TMOS).

(b) A mixture of $Fe(NO_3)_3{\cdot}9H_2O$ and an organometallic complex ($FeNa(EDTA){\cdot}2H_2O$) was used instead of the iron nitrate salt alone (sample B2).

Relevant data on sample preparation and characterization are shown in table 1.

Table 1. Aerogel alkoxide precursor and solvents, iron salt precursor, density (ρ), mean particle diameter (d_m) and standard deviation (σ_d) from TEM determination, activation energy (E) for magnetic moment reversal, microscopic attempt time (τ_0) from the ac susceptibility, effective anisotropy constant (K_{eff}) and magnetic phase identification.

Sample/ magnetic phase	Alkoxide and solvent	Iron salt precursor	ρ (g cm^{-3})	d_m (nm)	σ_d (nm)	E/k_B (K)	τ_0 (s)	K_{eff} (J m^{-3})
A1 ferrihydrite	TEOS ethanol	$Fe(NO_3)_3{\cdot}9H_2O$	0.52	2.4	1.6			
A3 maghemite	TMOS methanol	$Fe(NO_3)_3{\cdot}9H_2O$	0.44	5.0	1.3	1940	10^{-11}	1.02×10^5
B2 maghemite	TMOS methanol	$Fe(NO_3)_3{\cdot}9H_2O$+ $FeNa(EDTA) \cdot 2H_2O$	0.44	4.0	1.4	1700	10^{-11}	1.4×10^5

Besides the already published characterization of the materials, additional ME measurements were performed under transmission geometry with a standard constant acceleration spectrometer holding a ^{57}Co Rh radioactive source. Further x-ray diffraction (XRD) characterization was carried out with Cu Kα radiation in a Philips PW1710 diffractometer.

ac susceptibility measurements were performed in a Lake Shore 7130 susceptometer using a sample cup containing about 40 mg of material. To avoid nonlinear magnetization effects a low enough field $h_{ac} = 1$ Oe was used. Data were acquired at various frequencies $\omega/2\pi$ ranging from 5 to 9920 Hz. The temperature range 15–300 K was well below the ordering temperature (873 K) of the magnetic phase (maghemite). Therefore changes in saturation magnetization M_s are rather small, and so the M_s temperature dependence is neglected for ac susceptibility data analysis.

3. Results and discussion

The nanoparticle phase assignments were: maghemite (γ-Fe_2O_3) or magnetite (Fe_3O_4) for samples A3 and B2; and ferrihydrite ($Fe_5HO_8{\cdot}4H_2O$) for sample A1, according to Casas *et al* [8]. These assignations are based on XRD and Mössbauer measurements. XRD patterns allow an easy distinction between sample A1 and A3/B2: the first shows the typical six-line pattern of ferrihydrite, that behaves as a speromagnet [9, 10] (a material with the atomic spins frozen in random directions [11]); whereas samples A3 and B2 (pattern not shown) exhibit a pattern assignable to either magnetite or maghemite (figure 1) since both have a spinel-type structure. Mössbauer spectroscopy permits one to discriminate between the two phases. The room temperature spectra of both sample A3 (figure 2) and sample B2 are dominated by a superparamagnetic doublet. Their hyperfine parameters ($\Delta = 0.74(3)$ mm s^{-1} and $\delta_{Fe} = 0.36(2)$ mm s^{-1}) are consistent with those reported for superparamagnetic maghemite [12] and different from those of superparamagnetic magnetite [13]. The liquid nitrogen spectrum (figure 2 bottom) consists of a doublet, due to a fraction of superparamagnetic particles, superimposed on a magnetically split component. The slight asymmetry of the magnetic component (line 1 is deeper than line 6; see the inset in figure 2) is expected for maghemite [14], while the reverse situation should be found for magnetite, thus confirming the identification of the magnetic phase.

Thus, for the ac analysis we will assume that the iron-bearing phase within sample A1 is uniquely ferrihydrite and for samples A3 and B2 is uniquely maghemite. These assumptions

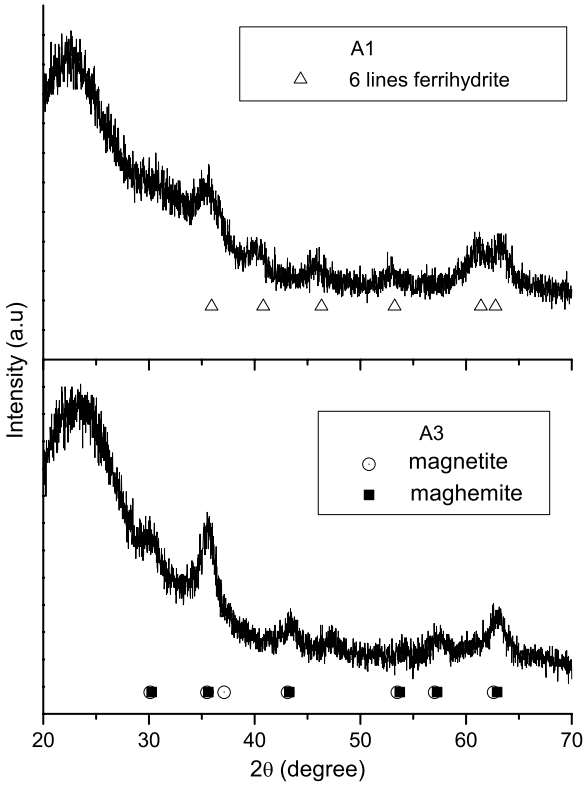

Figure 1. XRD powder patterns of A1 and A3.

built on published results and on additional measurements are central to the validity of the analysis. On the other hand, the coexistence of ferrihydrite and maghemite in a given sample is unlikely due to the different chemical contexts in which such phases occur.

Previous particle morphology studies showed a spherical shape for sample A1 and acicular morphology for samples A3 and B2. TEM micrographs and particle diameter (d) histograms shown in [8] are used to retrieve particle size data. Histograms are fitted to Gaussian functions (figure 3):

$$P(d) = (\sqrt{2\pi}\sigma_{\mathrm{d}})^{-1} \exp -0.5((d - d_{\mathrm{m}})/\sigma_{\mathrm{d}})^2 \tag{1}$$

where d is the short axis diameter of the acicular particles. Mean particle diameters d_{m} and standard deviations (σ_{d}) are listed in table 1. At higher diameter values the Gaussian fit is not so good, and underestimates the data. Then, a log-normal distribution, commonly used in colloid science, was tried. This function describes the histogram large diameter values better but the small ones for silica aerogel holding maghemite particles worse. The log-normal fits are also included in figure 3 for comparison. For the longitudinal axis of A3 and B2, only the average value of 20 nm was considered. In the case of ferrihydrite particles, a discrepancy between the log-normal fit and the experimental result is noticeable at both small and large diameter values.

Then, the samples studied here consist of nanosized (∼5–4 × 20 nm) acicular shaped maghemite particles (sample A3–B2) and spherical (∼2.5 nm) ferrihydrite (samples A1) [8] particles hosted in the porous silica aerogel structure (see table 1).

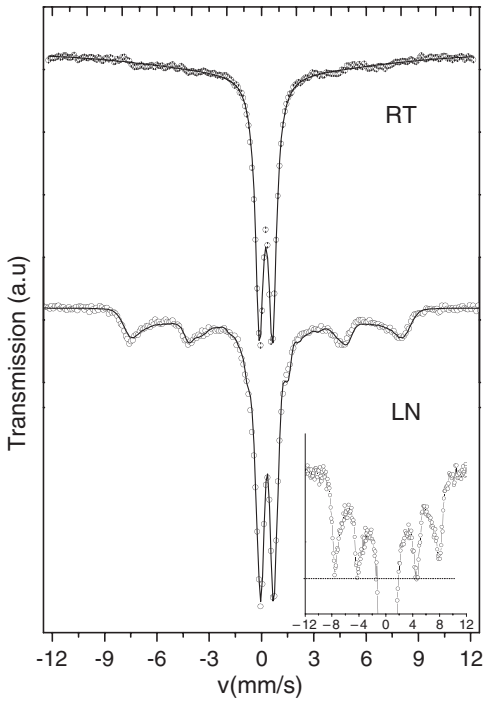

Figure 2. Room temperature (RT) and 77 K (LN) Mössbauer spectra of sample A3. Inset: close view of the magnetic component showing the asymmetry of lines 1 and 6.

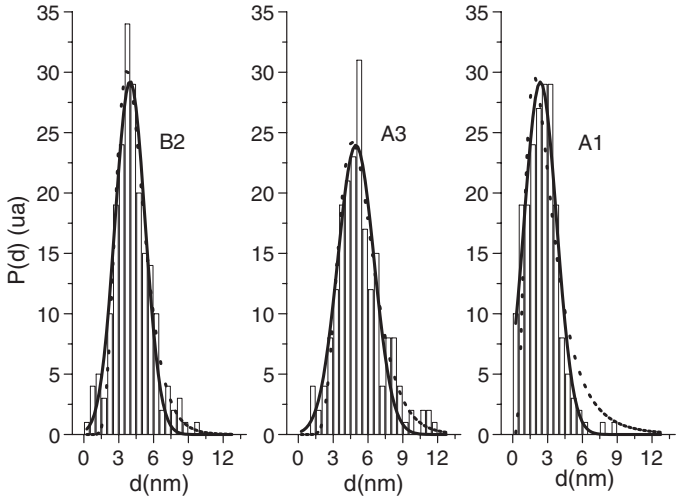

Figure 3. TEM histograms fitted with Gaussian (solid lines) and log-normal functions (dashed lines); for TEM pictures see [6].

The maghemite particle is a single magnetic domain, having a magnetization vector whose magnitude is essentially constant although its orientation fluctuates due to thermal agitation.

Figure 4 shows the thermal variation of the rescaled in-phase (χ') component of the first harmonic of χ_{AC} acquired at 825 Hz for samples A1, B2 and A3. The signal for A1 is very

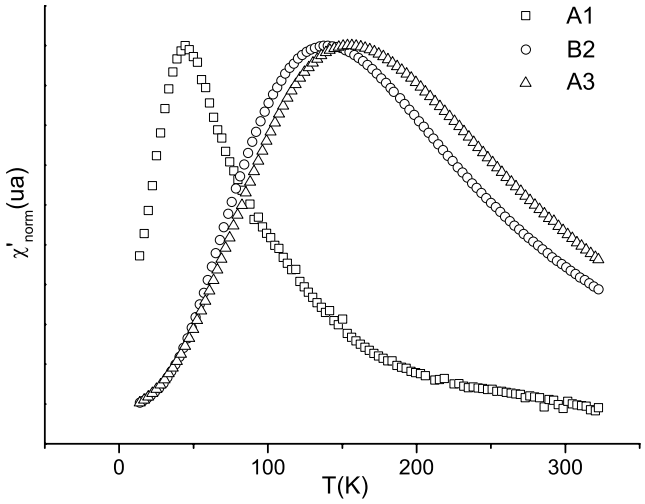

Figure 4. Temperature dependence of the in-phase (real) component $\chi'(T)$ for ferrihydrite/silica nanocomposite aerogel (A1) and for maghemite/silica nanocomposite aerogels (B2, A3).

weak (one order of magnitude weaker compared to those for A3 and B2), consistent with the speromagnetic behaviour of this sample and the extremely small size of the ferrihydrite particles. It has been argued [15] that for $d < 2$–3 nm the particle magnetization falls drastically. 56% of the particles have a diameter smaller than 2.3 nm. For samples A3 and B2 the results are similar, but the signal is stronger for A3, indicating a higher iron concentration compared to that of B2. This situation originates from a higher iron leaching during hypercritical drying for the sample B2. For both samples a population larger than 90% presents a diameter larger than 2.5 nm.

A3 and B2 samples exhibit the expected behaviour of a SPM system [16]. A well defined maximum appears in both in-phase χ' and out-of-phase χ'' susceptibility components at different temperatures T'_B and T''_B. The peak positions shift with increasing frequency to higher values (figure 5), as is typical for a rapid Arrhenius–Néel-like relaxation time $\tau = \tau_0 \exp(E/k_B T)$, where τ_0 is a microscopic attempt time whose magnitude is of the order of 10^{-9}–10^{-12} s; there is a weak temperature dependence [17], and E is the energy barrier that has to be overridden by the magnetic moments to change its orientation toward another energy minimum. In the simplest uniaxial anisotropic symmetry case [18] a unique energy barrier $E = KV$ appears, where K is the anisotropy constant of the particles.

According to the Néel model, we assumed that below T''_B most of the particle magnetic moments are blocked in fixed directions and equilibrium is not achieved. Here, τ follows from $\omega\tau(T''_B) = 1$, and plotting $1/T''_B$ against $\log(\omega/2\pi)$ straight lines are obtained, consistent with the Arrhenius law. In the literature τ is sometimes obtained from the maximum of $\chi'(\omega)$ [19] and sometimes from the maximum of $\chi''(\omega)$ [20, 21]. For our data, a large discrepancy between the Cole–Cole and Néel results is obtained if τ is derived from χ' analysis instead of χ''. Fitted values of τ_0 and E are listed in table 1.

As both blocking temperatures and E values scale with the mean particle volume V_m, corroborating the presence of magnetocrystalline anisotropy (see table 1), we write $E = K_{eff} V_m$, where K_{eff} is an effective anisotropy constant with other contributions besides magnetocrystalline anisotropy. Rather large values, $K_{eff} = 1.02 \times 10^5$ and 1.4×10^5 J m^{-3}, are obtained for A3 and B2 respectively, a fact which will be discussed below.

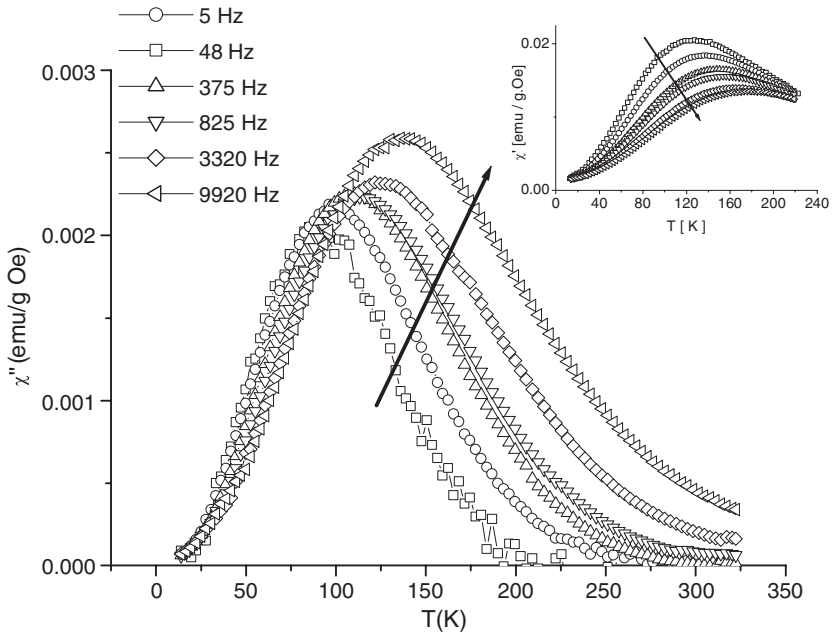

Figure 5. Temperature dependence of the out-of-phase (imaginary) component $\chi''(T)$ of the magnetic susceptibility for aerogel A3, at different excitation frequencies. Arrows indicate increasing frequencies. Inset: the in-phase (real) component $\chi'(T)$.

Next, we obtain the energy barrier distribution $g(E)$ as a consequence of the volume distribution. It is known that χ'' provides reliable information on τ and makes it possible to obtain values of τ_0 and the energy barrier distribution following a scaling procedure [22, 23]. This distribution is derived using the fact that, in the expression for $\chi''(T, \omega)$ for an ensemble of small particles,

$$\chi''(T, \omega) = \frac{C}{T} \int_0^\infty g(E) E \frac{\omega\tau}{1 + (\omega\tau)^2} \, \mathrm{d}E, \tag{2}$$

the function $\frac{\omega\tau}{1+(\omega\tau)^2}$ is peaked at $\omega = 1/\tau$, allowing us to take $g(E)E$ outside the integral and set it equal to $-k_B T \ln(\omega\tau_0) g(E)$. Then, plotting $\chi''(\omega, T)$ versus $-T \ln(\omega\tau_0) = E/k_B$ for all the frequencies, the data should collapse into a single curve when an appropriate τ_0 value is used. This plot provides the distribution function for the energy barriers. The best scaling plot was obtained using $\tau_0 = 10^{-11}$ s for both A3 and B2 samples in agreement with the previous Néel analysis.

Now, we test which of the $g(E)$ functions that follow from both particle size distributions (Gaussian and log-normal) matches the χ'' scaled data better. To do that, we start with formula (1), i.e. the Gaussian distribution analysis, and $E = K\frac{\pi d^2 l}{6}$. It follows that χ'' is proportional to the corresponding energy distribution given below:

$$\chi''(\omega, T) \propto E(\omega, T) g(E(\omega, T)) = A E^{1/2} \exp(-B(E^{1/2} - E_m^{1/2}))^2 \tag{3}$$

where E_m is the mean energy value, and A and B are parameters related to σ_d, K and l (the particle length). In figure 6 it can be seen that this function fits the scaled data, indicating a good agreement between volume distributions derived from TEM and obtained from ac susceptibility data. For instance, the $E_m = 1954 \pm 14$ K value obtained from the fit is in agreement with the values derived from the Arrhenius–Néel plot. The $g(E)$ function inferred

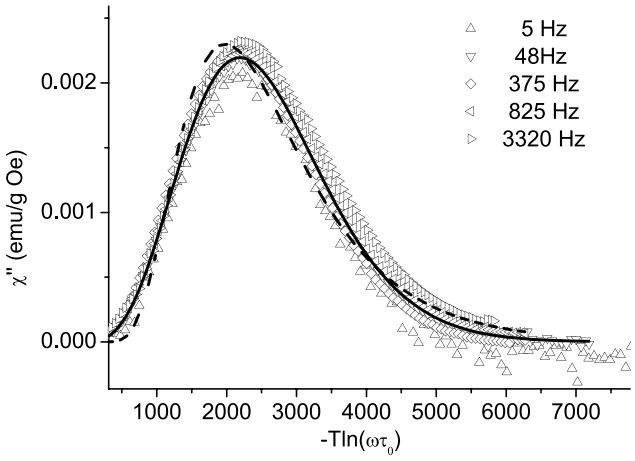

Figure 6. Out-of-phase (imaginary) part of the ac susceptibility for A3 aerogel plotted as a function of the scaling variable $\ln(1/\omega\tau_0)$ with $\tau_0 = 10^{-11}$ s. Solid lines are fits with a Gaussian (equation (2)) and dashed lines stand for fits with log-normal functions.

assuming a log-normal distribution is also plotted in figure 6. The fit with this function gives a chi square value 37 times worse than the one obtained with formula (3).

Depending on preparation parameters, aggregation of the magnetic particles may occur during nanocomposite aerogel synthesis and interaction between particles could be significant. To determine the presence of magnetic interparticle interactions we used the frequency sensitivity criterion [24] $S = \frac{\Delta T_B}{T_B \Delta \log(\omega/2\pi)}$ which gives 0.105 ± 0.005 and 0.113 ± 0.003 for A3 and B2 respectively, indicating isolated, non-interacting particle behaviour. The application of the Vogel–Fulcher criterion [24] also indicates the absence of particle interactions.

From the nominal mass quotient $R = m_{Fe}/m_{Si}$, sample density ρ, maghemite density $\rho_{Fe_2O_3}$ and V_m, the mean separation between particles calculated for various configurations can be estimated as $d_{PP} \cong 14.5$ nm for A3. As the Fe which leaches during hypercritical drying of the gels cannot be quantified, d_{PP} was estimated using R; the lower the R value, the higher the d_{PP} values. For $d_{PP} \geqslant 10$ nm no interaction between nanometre size particles is expected [25].

An alternative approach for obtaining $\tau(T)$, which is the main difference compared to other approaches used here, is that no specific dependence on the volume distribution function or on the corresponding $g(E)$ function is assumed, not even through the Neél equation; we use of the phenomenological Cole–Cole expression from [26]:

$$\chi(\omega) = \chi_S + \frac{\chi_T - \chi_S}{1 + (i\omega\tau_m)^{1-h}} \tag{4}$$

in which χ_T and χ_S are the isothermal (superparamagnetic) and adiabatic susceptibilities, respectively, and τ_m is the mean relaxation time. This expression is obtained from

$$\chi(\omega) = \int \frac{\tau G(\tau)}{1 + i\omega\tau} \, d(\ln \tau) \tag{5}$$

if a proper function $\tau G(\tau)$, symmetric around $\tau = \tau_m$ is used, where $G(\tau)$ is the relaxation times distribution, and h determines the width of the distribution: $h = 1$ corresponds to an infinitely wide distribution, while for $h = 0$, equation (4) reverts to the equation appropriate for relaxation with a single time constant. Within this framework, data analysis can be realized by producing a plot of $\mathrm{Im}(\chi(\omega))$ against $\mathrm{Re}(\chi(\omega))$, known as an Argand plot—a circular and an elliptic arc form may be obtained for $h = 0$ and $h \neq 0$ respectively [21]—or by

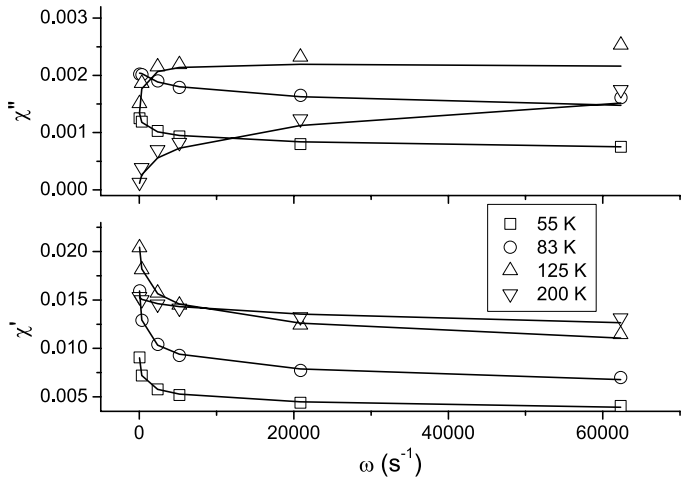

Figure 7. ac susceptibility frequency dependence for aerogel A3 (bottom: $\chi'(\omega)$; top: $\chi''(\omega)$) for the five frequency excitation values used at various temperatures. The solid line stands for the simultaneous fit using real and imaginary parts of equation (3).

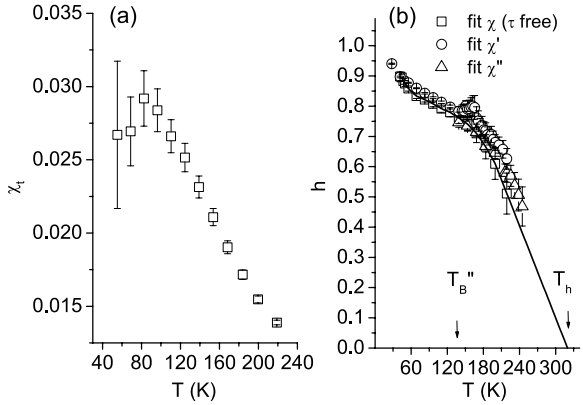

Figure 8. (a) Isothermal susceptibility χ_T obtained from the simultaneous fit, using the Cole–Cole expression, of χ' and χ'' data plotted in figure 7. (b) The Cole–Cole parameter h as a function of temperature for maghemite/silica nanocomposite aerogel A3.

fitting the frequency dependence of the real and imaginary parts of equation (4), at constant temperatures, simultaneously to $\chi'(\omega)$ and $\chi''(\omega)$ experimental data with χ_T, χ_S, τ_m and h as adjustable parameters.

In figure 7 the simultaneous fits of real and imaginary parts of the frequency dependence of equation (4), are shown for sample A3. The analysis was performed for a large discrete set of temperatures but, for clarity, is only shown for five constant temperatures. A representative temperature dependence of χ_T, h is shown in figures 8(a) and (b).

The fitted χ_S value was zero within the experimental accuracy in all cases, indicating that the anisotropy field rather than the external field dominates the initial response of the particle moment. Therefore, it was fixed to zero to reduce the number of fitting parameters. χ_T decreases monotonically with increasing temperature above 80 K as expected for the superparamagnetic susceptibility. Large errors were obtained for this parameter below 75 K.

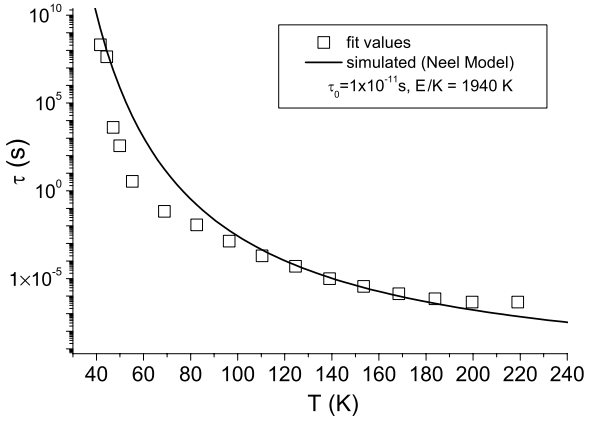

Figure 9. Temperature dependence of the Cole–Cole mean relaxation time τ_m (square symbols) and the Néel model (solid line) for aerogel A3.

The behaviour of h is similar to the one reported for EuSrS spin glasses [27]. This parameter varies slowly and almost linearly between 40 and 140 K, and then the slope becomes more pronounced. h indicates the deviation of the relaxation time from a single time constant. Extrapolating h to find the intersection with the temperature axis indicates that above 320 K the system would behave as non-distributed (the width of the relaxation time distribution negligible as compared with the relaxation time itself). The cause of the break in the $h(T)$ curve is still unclear, but it is noticeable that it appears at a temperature slightly higher than the maximum blocking temperatures obtained from the maxima of χ''.

The mean relaxation time temperature dependence $\tau_m(T)$ as obtained from these fits is shown in figure 9 for A3. The solid line represents the relaxation time simulated with the Néel model for $\tau_0 = 10^{-11}$ s and $E/K = 1940$ K. The comparison suggests that the dynamics of the system may not follow the simple Néel behaviour, especially within the temperature range 50–100 K. An alternative fit of the $\chi(\omega)$ real and imaginary components was carried out keeping the relaxation times fixed at the values predicted from the Néel model. Only the fitted values of χ_T depart considerably (up to 50%) from those obtained in the previous fits in the temperature interval where the τ discrepancy was observed, while the general behaviours of h follow the same trend in the two cases. Moreover the same $h(T)$ behaviour was obtained from fitting the real and imaginary parts independently (as can be seen in figure 8(b)). This is an important result because for some combinations of frequency and temperature the values of χ'' were obtained with less reliability in the case of sample B2. Then, for this sample only, the fit of the real part was performed. The h comparison between A3 and B2 is shown in figure 10.

Argand diagrams for the A3 sample are shown in figure 11. Values of χ_T, χ_S, τ_m and h obtained from the fit of the elliptic arc are in agreement with real and imaginary frequency dependence fits.

The blocking temperature is not a physical quantity, in the sense that it depends on the experimental temporal window t_{exp}; for instance $t_{exp} \cong 10^{-5} - 10^{-1}$ s and $t_{exp} \cong 10^{-8}$ s for χ_{ac} and ^{57}Fe Mössbauer effect experiments respectively. Depending on whether t_{exp} is smaller or larger than τ, the particle magnetic moment may be seen as blocked or fluctuating. Nevertheless, blocking temperature measurements allow the determination of the relaxation time, which is the important physical parameter; thus information from different experiments should match. In figure 12 relaxation time–temperature dependence values as obtained from Néel analysis of χ'' extrapolated to room temperature, Cole–Cole frequency dependence

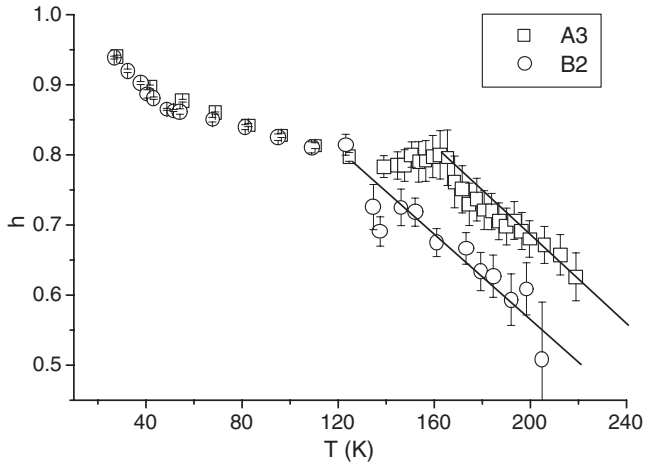

Figure 10. The Cole–Cole parameter h as a function of temperature for maghemite/silica nanocomposite aerogels A3 and B2.

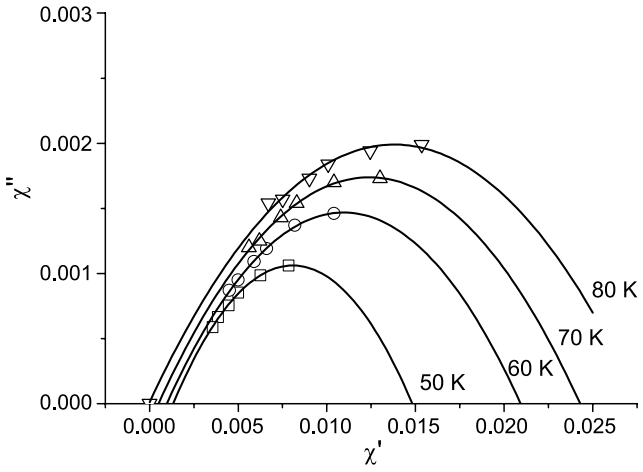

Figure 11. Argand diagram for maghemite/silica nanocomposite aerogel A3 at selected temperatures.

analysis (both Argand plots and the fit as described above) and a value derived from the ME room temperature data are plotted. It must be pointed out that a difference as big as $\Delta \log \tau > 2$ is obtained between Cole–Cole results and Néel results if the latter are derived from χ' analysis instead of χ''.

As mentioned before, the values derived for K_{eff} are two orders of magnitude larger than the bulk magnetocrystalline anisotropy constant of maghemite [28] (4.8×10^3 J m^{-3}). Besides the magnetocrystalline anisotropy contribution to E, shape and/or stress anisotropy may appear. For A3 and B2 samples, TEM data [8] indicate acicular shapes with mean particle sizes of 5 nm $\times$ 20 nm and 4 nm $\times$ 20 nm respectively. For acicular shape, $K_{\text{shape}} = \frac{\mu_0}{2}(N_a - N_c)M_{\text{s}}^2$ with N_a and N_c the demagnetization factors along the minor and major axes and M_{s} the saturation magnetization. For our cases, K_{shape} equals 1.3×10^3 J m^{-3} for A3 and is larger for B2 although of the same order. These values are also two orders of magnitude smaller

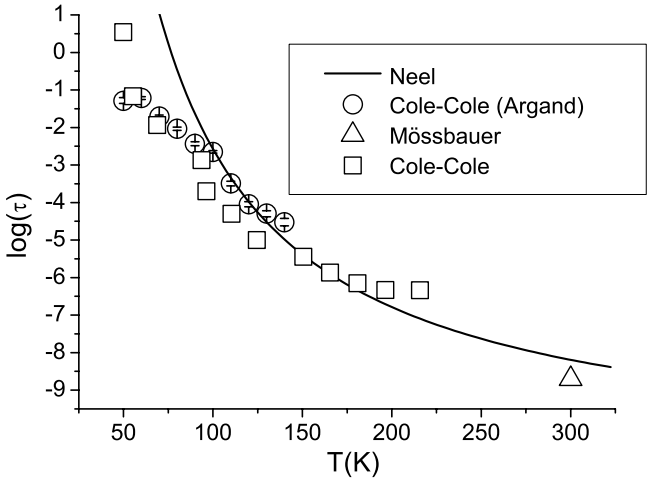

Figure 12. Comparison between Cole–Cole and Néel analysis of the ac susceptibility for maghemite/silica nanocomposite aerogel A3. The open triangles stand for Mössbauer effect data.

than the measured ones. Stress anisotropy can be neglected because the magnetic particles are nanometric in size and hosted in pores, which are larger than the particles. Interparticle interactions (dipolar or exchange) can also modify the energy barrier [29] but they are not expected in our case as all the classifying criteria applied to our data indicate non-interacting particles. Thus, the origin of this extra anisotropy must be related to the large amount of atoms at the periphery of the particle. As magnetocrystalline anisotropy originates from the spin–orbit interaction, the 3d electrons of the atoms located at the surface [7] are likely to have an increasingly localized character; consequently they have larger orbital moments, giving rise to this extra anisotropy. The following phenomenological size dependence of the effective anisotropy, which takes into account that K_{eff} scales with the fraction of atoms at the periphery of the particle, has been established [30]: $K_{\mathrm{eff}} = K_{\mathrm{B}} + \frac{\gamma K_{\mathrm{s}}}{d_{\mathrm{m}}}$, where K_{B} and K_{s} are the volume and surface anisotropy energy densities, and γ/d_{m} is the surface to volume ratio. For our data, a K_{s} value of 1.26×10^{-4} J m^{-2} is obtained. This value is of the same order of magnitude as the ones derived for α-Fe nanoparticles on carbon supports [30] and Co clusters in Al_2O_3 [7], equal to 0.9×10^{-4} and 3.3×10^{-4} J m^{-2}, respectively.

4. Conclusions

We have presented a detailed analysis of ac susceptibility measurements of iron oxide/silica aerogel nanocomposites prepared by the sol–gel method and supercritical drying of the gels. Depending on the synthesis parameters, ferrihydrite or maghemite particles are obtained. It is found that aerogels hosting maghemite particles behave as superparamagnets without interparticle interaction. The microscopic attempt time $\tau_0 = 10^{-11}$ s gives the best scaling of the out-of-phase ac susceptibility and effective values for the anisotropy constant of 1.02 and 1.4×10^5 J m^{-3}, for 5 nm $\times$ 20 nm and 4 nm $\times$ 20 nm average dimensions of acicular particles. These K_{eff} values are enhanced with respect to the bulk and are proportional to the amount of atoms located at the surface of the particles, giving a surface contribution to K_{eff} of 1.26×10^{-4} J m^{-2}. The absence of interparticle interactions allows one to corroborate that this synthesis path is very effective at preventing particle aggregation. Finally, distinctive analyses

of the ac susceptibility signal, Néel using χ'', scaling procedure on χ'', Cole–Cole frequency dependence (both Argand plots and fit using the analytic expression) give a consistent relaxation time–temperature dependence, which also agrees with a value derived from Mössbauer effect spectroscopy.

Acknowledgments

This research was supported by CONICET of República Argentina. Financial support from Carburos Metálicos S.A. and the Spanish Ministry of Science and Education MAT2003-01052 is acknowledged.

References

[1] Casas Ll, Roig A, Molins E, Greneche J M, Asenjo J and Tejada J 2002 *Appl. Phys.* A **74** 591
[2] Popovici M, Gich M, Roig A, Casas Ll, Molins E, Savii C, Becherescu D, Sort J, Suriñach S, Muñoz J S, Baró M D and Nogués J 2004 *Langmuir* **20** 1425
[3] Clapsaddle B J, Gash A E, Satcher J H, Hrubesh L W and Simpson R L 2001 *J. Non-Cryst. Solids* **285** 22
[4] Cannas C, Casula M F, Concas G, Corrias A, Gatteschi D, Falqui A, Musinu A, Sangregorio C and Spano G 2001 *J. Mater. Chem.* **11** 3180
[5] Gich M, Casas Ll, Roig A, Molins E, Sort J, Suriñach S, Baró M D, Muñoz J S, Morellon L, Ibarra M R and Nogués J 2003 *Appl. Phys. Lett.* **82** 4307
[6] Leventis N, Elder I A, Long G J and Rolison D R 2002 *Nano Lett.* **2** 63
[7] Luis F, Torres J M, García L M, Bartolomé J, Stankiewicz J, Petroff F, Fettar F, Maurice J L and Vaurés A 2002 *Phys. Rev.* B **65** 094409
[8] Casas Ll J, Roig A, Rodríguez E, Molins E, Tejada J and Sort J 2001 *J. Non-Cryst. Solids* **285** 37
[9] Murad E 1988 *J. Magn. Magn. Mater.* **74** 153
[10] Murad E and Schwertmann U 1980 *Am. Mineral.* **65** 1044
[11] Coey J M D 1993 *J. Phys.: Condens. Matter* **5** 7297–300
[12] Ninjbadgar T, Yamamoto S and Fukuda T 2004 *Solid State Sci.* **6** 879–85
[13] Goya G F 2004 *Solid State Commun.* **130** 783
[14] Mørup S, Bødker F, Hendriksen P V and Linderoth S 1995 *Phys. Rev.* B **52** 287
[15] Raikher Y and Shliomis M 1994 *Adv. Chem. Phys.* **87** 607
[16] Dormánn J L, Fiorani D and Tronc E 1997 *Adv. Chem. Phys.* **XCVIII** 326
[17] Brown W F 1963 *Phys. Rev.* B **130** 1677
[18] Néel L 1949 *Acad. Sci. Paris* **228** 664
[19] Dormann J L, Cherkaoui R, Spinu L, Noguès M, Lucari F, D'Orazio F, Fiorani D, García A, Tronc E and Jolivet J P 1998 *J. Magn. Magn. Mater.* **187** L139
Voit W, Kim D K, Zapka W, Muhammed M and Rao K V 2001 *Mater. Res. Symp. Proc.* **676** y8.3
[20] Wiekhorst F, Shevchenko E, Weller H and Kötzler J 2003 *Phys. Rev.* B **67** 224416
Sorop T G, Evangelisti M, Haase M and Jongh L J 2004 *J. Magn. Magn. Mater.* **273/274** 1573
[21] Fannin P C and Charles S W 1995 *J. Phys. D: Appl. Phys.* **28** 239
[22] Slade S B, Gunther L, Parker F T and Berkowitz A E 1995 *J. Magn. Magn. Mater.* **140–144** 661
[23] Jonsson T, Mattsson J, Nordblad P and Svedlindh P 1997 *J. Magn. Magn. Mater.* **168** 269
[24] Dormánn J L, Spinu L, Tronc E, Jolivet J P, Lucari F, D'Orazio F D and Fiorani D 1998 *J. Magn. Magn. Mater.* **183** L255
[25] Luis F, Petroff F, Torres J M, García L M, Bartolomé J, Carrey J and Vaurès A 2002 *Phys. Rev. Lett.* **88** 217205
[26] Cole K S and Cole R H 1941 *J. Chem. Phys.* **9** 341
[27] Baalbergen J J 1987 *PhD Thesis* Leiden
[28] Vassiliou J K, Mehrotra V, Russel M W, Giannelis E P, McMichael R D, Shull R D and Ziolo R F 1993 *J. Appl. Phys.* **73** 5109
[29] Goya G F, Fonseca F C, Muccilio R, Carreño N L V, Longo E and Leite E R 2003 *J. Appl. Phys.* **93** 6531
[30] Bødker F, Mørup S and Linderoth S 1994 *Phys. Rev. Lett.* **72** 282